ARTICLE

Thermal prestressing of subsequently slotted reinforcement—Experimental and numerical development and optimization of an induction method

Yannik Schwarz[1] | Denis Ratke[2] | David Sanio[1] | Thomas Meurer[2] | Peter Mark[1]

[1]Institute of Concrete Structures, Ruhr University Bochum, Bochum, Germany

[2]Karlsruhe Institute of Technology, Digital Process Engineering, Karlsruhe, Germany

Correspondence
Yannik Schwarz, Ruhr-University Bochum, Institute of Concrete Structures, 44780 Bochum, Germany.
Email: yannik.schwarz@rub.de

Abstract

Many infrastructure buildings show deficits in their load-bearing capacity and need to be strengthened in the short or medium term. However, the available methods are usually not effective for the self-weight without temporary raising or prestressing the structure. To resolve this problem, thermal prestressing of slotted reinforcing bars is proposed here. The bars are embedded in a grouting material tempered from the outside and thermally expanded according to the temperature change. When the heat supply is stopped, the bond with the hardened grouting material restricts the re-deformation of the bars during cooling. This creates prestress that counteracts the bending moment from the self-weight and relieves the tensile zone of the cross-section. Of course, it is important to limit the heat input to the slots when tempering. Heating the entire cross-section would reduce the effectiveness of the strengthening. The paper shows the experimental and numerical development of an induction method to thermally prestress subsequently added slotted reinforcement. The strengthening method is first implemented experimentally in reference tests with varying slot shapes. The results are then used to calibrate a numerical computation that is used to investigate the influence of other boundary conditions on the effectiveness of the strengthening measure. The optimum result is derived therefrom and experimentally validated, taking into account practical construction needs. The results show that the numerical optimization of the induction method increases the effectiveness of the strengthening by up to 100%. Accordingly, the reinforcing bars must be installed in triangular, 10 cm wide slots filled with high-strength concrete (HPC), which is tempered with the highest available thermal output and up to 95°C. In order to counteract the temperature increase in the concrete at the initial cross-section, which reduces

the effectiveness, it must be cooled in parallel. It is advisable to place dry ice at a distance of 6 cm from the edge of the slot over the largest possible width. For practical realization of the strengthening with usually several bars added in parallel, a minimum bar spacing of 40 cm must be maintained to ensure sufficient cooling between the slots. Alternatively, the bars should be attached and thermally prestressed in sequence.

KEYWORDS

computation of temperature fields, optimization, post-installed reinforcement, strengthening, thermal induction, thermal prestress

1 | INTRODUCTION

In view of the aging of buildings and infrastructure, strengthening of reinforced concrete structures is becoming increasingly important.[1] The demand is high, especially for infrastructure buildings such as bridges.[2] It is estimated that approx. 50% of the bridge structures in Germany and approximately 40% in the US[3] have calculated deficits in their load-bearing capacity and need to be strengthened or replaced in the short or medium term.[4] Among the reasons for this are increased stresses and design loads, changes in the regulations for design and construction, as well as damage caused by environmental influences such as corrosion of the reinforcing bars.[5,6]

Strengthening offers ecological and economic advantages compared to replacement.[7] Available structural resources can be used efficiently, reducing the total amount of building materials and energy required as well as CO_2 emissions. In addition, the long execution times for replacement structures often lead to heavy traffic congestion.[6,8] In addition to the already high planning and execution costs, this causes further indirect costs, such as macroeconomic effects as a result of impaired traffic networks and CO_2 emissions due to congestion, longer traffic routes, and traveling times and associated emitted pollutants.[6,8] Indirect costs cause the majority of the ecological and economic impact of infrastructure construction measures and clearly outweigh the direct costs.[9]

To strengthen deficits in the flexural load-bearing capacity, typical methods include enlarging the compression zone with additional concrete[10] or strengthening the tension zone with slotted reinforcement,[11,12] bonded steel plates,[13–15] or CFRP fabrics.[16–18] However, all these methods are not effective for the imposed dead loads without temporary lifting with additional supports or prestressing of the structure.[19,20] Since the dead load of reinforced concrete bridges, for example, accounts for around 70%–80% of the total load,[21] the effectiveness of the

methods in the serviceability limit state (SLS) remains low.

Reinforcement can be activated for the self-weight by imprinting constrained internal forces in statically indeterminate systems as a result of targeted tempering.[22–25] These internal forces, that is, bending moments from linear temperature gradients, counteract the effects of self-weight, temporarily reducing stresses in the initial structure and allowing reinforcement to be applied in this preloaded state. After stopping the heat supply and cooling, the dead load is redistributed between the initial cross-section and the reinforcement. Alternatively, and especially in statically determinate systems, activation can be achieved by targeted thermal prestressing of subsequently added reinforcement; analogous to the conventional post-tensioning method by subsequent bonding. Figure 1 shows the strengthening principle at the example of a single-span plate girder bridge, whose tension zone is strengthened under dead load g by two slotted reinforcement bars with the cross-sectional area A_s. The bars are added to the bottom face in subsequently made slots between the existing reinforcement (A_{s0}). The slots are filled and immediately tempered from the outside to thermally stretch the bars according to the temperature change $\Delta\vartheta$ by the strain ε_s and to match the strain of the initial reinforcement ε_{s0} induced by g. After the grout has hardened, temperature induction stops. The bond between the steel and the grout prevents the subsequently added bars from re-shaping and a compressive force F_{PT} is created as well as a bending moment due to their distance from the barycenter of the cross-section. This counteracts the stresses from the self-weight and relieves the tensile zone of the existing cross-section.[26] The added reinforcing bars are thus effective for the self-weight.

The main challenge is to limit the heat input to the slots. An increase in temperature in the initial cross-section reduces the temperature difference to the slot and thus the effectiveness of thermal prestressing.[26]

FIGURE 1 Strengthening principle with subsequently slotted and thermally prestressed reinforcement.
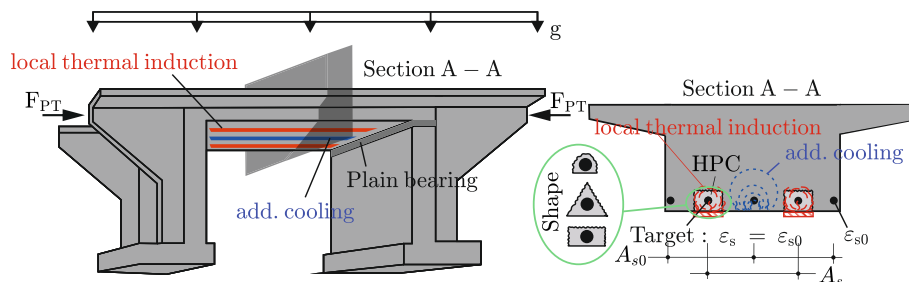
Simultaneous lateral cooling of the initial cross-section can counteract the heat transfer. The position and intensity of the cooling must be such that the initial cross-section is effectively cooled without significantly reducing the temperature development in the slot. The temperature distribution in the cross-section when the grout has sufficiently hardened to transfer the bond stresses from thermal prestressing is decisive for the effectiveness of the strengthening. From then, the thermal stretching is permanently imprinted and further temperature changes no longer have any influence on the pre-strain. Thus, rapid hardening grouts and high heating rates are to be combined at best. The grout must be suitable for tempering without pre-storage time.[27,28]

The proposed method offers a significant advantage over conventional strengthening techniques by directly activating the added reinforcement for the self-weight, increasing its efficiency in the serviceability limit state. The prestressing can close existing cracks in the concrete and reduce deflection. However, compared to conventional reinforcement additions without thermal prestressing, this approach is more complex in execution and requires precise planning as well as careful control of the heating process on the construction site. Then, it provides an innovative and efficient solution for enhancing the performance and durability of reinforced concrete structures.

The paper shows the experimental and numerical development as well as optimization of an induction method for thermal prestressing of subsequently added reinforcement. The influence of different slot shapes on the temperature evolution of the added bars and the grout as well as the heat propagation to the initial cross-section is investigated experimentally on unloaded specimens (Sections 2 and 3). The most advantageous shape is selected and mapped in a numerical model for further investigations. In this model, the impact of simultaneous cooling of the initial cross-section and different thermal and geometric boundary conditions on the effectiveness of the strengthening measure is investigated (Section 4). The results are used to derive the optimum induction method in terms of cooling and heating geometry, considering practical construction aspects, and validated in a final experiment (Section 5).

2 | EXPERIMENTAL INVESTIGATIONS ON THE SHAPE OF SLOTS

2.1 | Test campaign

In the tests, the influence of the slot shape on the temperature evolution in the added bar and the heat propagation to the initial cross-section is investigated. For this purpose, the strengthening method is implemented on unloaded specimens with varying slot shapes, then the temperature development in the specimen is measured. The aim is to gain a temperature difference between the added reinforcement and the concrete of 60°C, which corresponds to a thermal pre-strain $\varepsilon_s = 0.6\%o$ at $\alpha_T = 10^{-5}$ $(1/K)$ (coefficient of thermal expansion for steel and concrete). This is required on average for standard reinforced concrete structures with about 70% dead load contribution so that $\varepsilon_s = \varepsilon_{s0}$ applies.[26] Assuming an initial temperature of 20°C, the slot must therefore be heated to 80°C.

The specimens consist of normal strength concrete of class C30/37. A high-strength concrete (HPC) based on the binder Nanodur Compound 5941 is used to fill the slots in accordance with the requirements defined in Section 1.[29–31] Preliminary work shows that for this HPC, a rapid heat treatment without pre-storage makes the bond strength evolve fast,[8,28] without relevant damage due to secondary ettringite formation.[32] Approximately 65% of the maximum bond strength is reached in just 4 h.[28] In addition, the long-term deformations from creep and shrinkage in HPC, which lead to a reduction in the applied prestressing force,[28] are low and are even further reduced by the heat treatment.[28,33] Table 1 shows the compositions of the concretes used.

The test campaign is summarized in Table 2. In series 1 on the influence of the slot shape, the reinforcement is installed competitively on specimens with rectangular, triangular, and semicircular slots. The temperature of the slots is controlled from the outside using a heating mat (target temperature 80°C). Accompanying cooling of the initial cross-section is initially omitted.

For the most effective slot shape, a cooling concept is developed from a numerical model, and the slot

TABLE 1 Concrete compositions for normal concrete (initial cross-section) and HPC (slot).

Component	Normal concrete C30/37		HPC based on Nanodur compound 5941	
	Type	Mass [kg/m^3]	Type	Mass [kg/m^3]
Sand	0/2	711.0	0/2	426.0
Basalt	-	-	1/3	882.0
Gravel	2/8	356.0	-	-
Gravel	8/16	711.0	-	-
Binder	CEM 1 42.5 R	340.0	Nanodur compound 5941	1042.0
Water		204.0		159.8
Superplasticizer	-	-	Master Glenium ACE 430	12.3
Shrinkage reducer	-	-	Eclipse floor	8.0
Hardening accelerator	-	-	Master X-seed 100	12.3

TABLE 2 Test campaign.

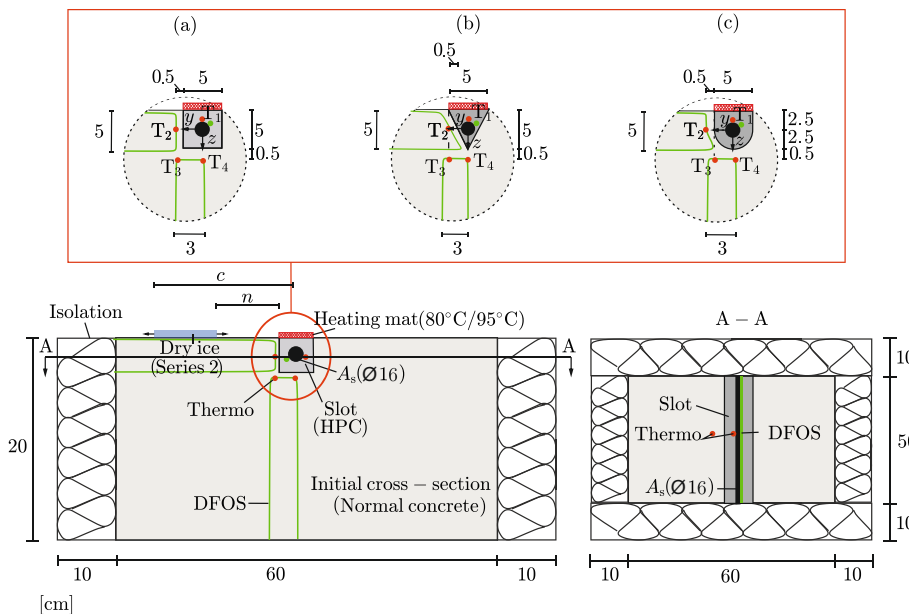| Test series	Slot shape	Target temperature heating mat [°C]	Lateral cooling	Number of samples
(1) "Influence slot shape"	Rectangle	80	-	1
	Triangle			1
	Semicircle			1
(2) "Optimized structure"	Triangle	95	According to Section 4	1

FIGURE 2 Principle design of the stand for the slot shapes (a) rectangular, (b) triangular, and (c) semi-circular along with the measurement equipment without (series 1) and with cooling (series 2).

dimensions are optimized (Section 4). The numerically optimized solution is implemented in a further experiment for validation in series 2. Due to reduced effectiveness, as found in series 1, the target temperature of the heating mat is increased to 95°C here. Everything else remains unchanged between the two series.

2.2 | Experimental setup and execution

The test setup with the geometric dimensions and the measurement equipment used is shown in Figure 2. The specimens have the dimensions $b/l/h = 60/50/20$ cm and are thermally insulated on all sides by a 10 cm thick polystyrene insulation ($\lambda = 0.04$ W/mK). The top and

bottom of the samples are open, allowing direct heat exchange with the environment.

As purely thermal tests are concerned, the specimens are initially unreinforced. The reinforcement is added in the form of a Ø16 bar with the area A_s in a (a) rectangular, (b) semicircular and (c) triangular slot (Figure 2, top). All slots are 5 cm wide (b') and 5 cm deep (h') regardless of shape. The reinforcement is placed at the center of the slot ($b'/2, h'/2$). The slots are filled with the HPC according to Table 1 and tempered with a silicone heating mat with the same dimensions as the slot surface. The heating mat has a two-point controller and a temperature sensor to keep the specified target temperature constant, cf.[34] A heat-resistant Hostaphan film ($t = 0.05$ mm) is placed between the heating mat and the liquid concrete to protect the mat.[27] The mat is heated to a target temperature of 80°C in series 1. In series 2, the target temperature is increased to 95°C and the experimental setup is enhanced to include laterally offset cooling on the upper side of the initial cross-section with dry ice (-78°C). The clear distance of the cooling to the heating mat n and the cooling width, which is clearly defined by the distance c between the center of the slot and the outer edge of the cooled area (see Figure 2 bottom left) as well as n and b, are determined according to the numerical optimizations in Section 4.

Due to symmetry of the cross-section, the instrumentation is only arranged on one half (series 1 and 2). The temperature evolution on the added bar is recorded selectively at $l/2$ with a thermocouple (T_1) and quasi-continuously over the length of the bar with a glass fiber (DFOS).[35–37] The DFOS is decoupled from the mechanical strains of the bar through installation in a capillary and therefore only records thermal strains, from which the temperature change to the initial state can be derived. The distance between the discrete measuring points (equivalent to the gauge length) on the fiber is 2.6 mm. The accuracy of the strain measurement using DFOS is approximately 0.03‰ and of the temperature measurements ± 0.4°C.[38] The measurements of all thermocouples and DFOS are carried out in a frequency $f = 1/10$ Hz.

The temperature evolution in the concrete is recorded at three points in the middle of the sample ($l/2$) via thermocouples ($T_2 - T_4$). The placement of the thermocouples is adapted to the slit geometry (Figure 2, top). The exact position of the thermocouples in the cross-section is defined by the distances in the y and z directions in relation to the barycenter of the added reinforcement. For all slot shapes T_2 is placed at the height of the added bar ($z = 0$ cm) and 0.5 cm from the edge of the slot. The distance in the y-direction to the reinforcement layer is therefore 3 cm for the rectangular and semicircular shapes and 1.75 cm for the triangular shape. The

positions of T_3 and von T_4 are independent of the slot shape at $y = 3$ cm, $z = 3$ cm or $y = 0$ cm, $z = 3$ cm.

Moreover, the temperature evolution is recorded with two DFOS running arc-like close to the thermocouples. The first (lateral) sensor runs in two layers parallel to the cross-section surface, the upper one at a distance of 0.5 cm from the surface, the lower one at the level of the bottom of the slot. In between the DFOS is bent with radii of 1 and 2 cm, depending on the shape of the slot. It runs parallel to the side face of the slot at a distance of 0.5 cm. The lower DFOS runs vertically towards T_3 and T_4. Between the thermocouples, the DFOS is again bent with a radius of 1 cm and runs horizontally. In order to be able to assign a unique position in the cross-section to each measuring point on the fiber, the start and end points of the bent length are identified with the so-called hot-spot method.[27,34] This means, the points are heated locally with a hot needle before concreting and thus made visible during the ongoing measurement and their position is saved. Using the known bending radii, the exact position can be calculated for each measuring point based on the marked points.[27] As the DFOS only records temperature-related strain changes in relation to an initial state, the sensors are calibrated with the absolute measured values of the thermocouples at the start of the measurement.

Figure 3 shows the test procedure with the main steps. In the first step (Figure 3a), the thermocouples and DFOS are fixed at the appropriate positions in the cross-section (see Figure 2) using wires (Ø 1.5 mm) stretched between the formwork panels. The slots are created during the concreting of the specimen using polystyrene void formers, which are fixed in position during concreting and secured against floating. In the second step (Figure 3b), the formwork is filled with the normal strength concrete according to Table 1. The void former is removed after hardening. The reinforcement is then added together with the appropriate measuring equipment on the bar. In the next step, the slot is filled with the HPC and tempered with a silicone heating mat for approximately 5 h (Figure 3c). The results in[28] show that the HPC is sufficiently hardened after this tempering time and is able to transfer the bond stresses from thermal prestressing.

3 | EXPERIMENTAL RESULTS AND DISCUSSION

3.1 | Evolution of temperature in the specimen with respect to the shape of the slot

The temperature evolution in the specimen, recorded with thermocouples ($T_1 – T_4$), is shown in Figure 4 as a
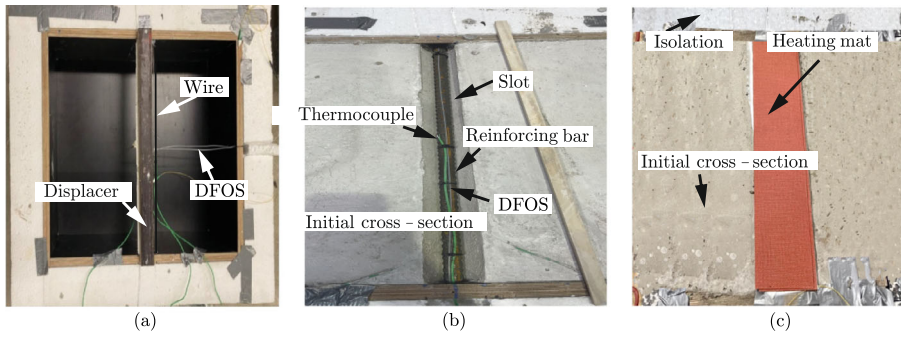
FIGURE 3 Steps of test execution: attaching measuring equipment (a), placing the bars (b), and grouting the voids and applying the heating mat (c).
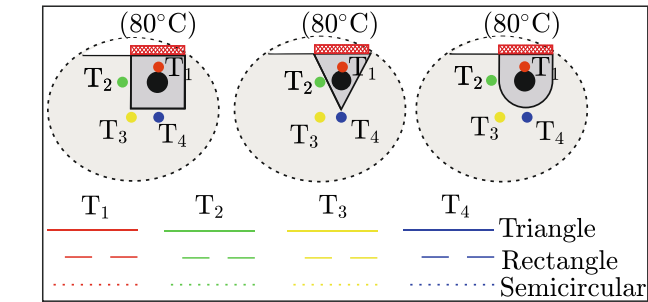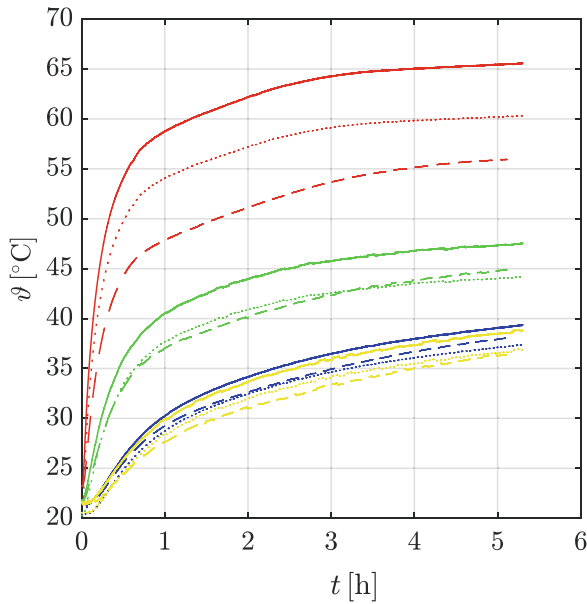

FIGURE 4 Measured temperature evolution in the slot and the initial cross-section as a function of the slot shape, recorded using thermocouples.
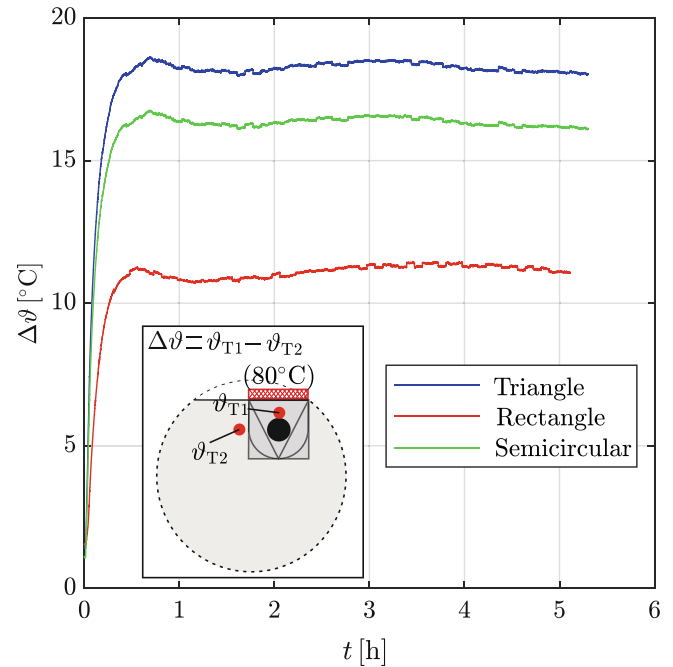

FIGURE 5 Temporal evolution of the temperature difference between slot and concrete (measuring point T_2) as a function of the slot shape, derived from the temperature measurements in Figure 4.

function of the slot shape. The solid lines show the results for the triangular shape, the dashed lines for the rectangular one and the dotted lines for the semicircular one. The added bar (T_1), shown in orange, heats up the most in the triangular shape at the end of the investigated time period ($t = 5$ h) (66°C), followed by the semicircular (60°C) and the rectangular (56°C). The temperature increase in the initial cross-section ($T_2–T_4$) is also highest for the triangular slot shape (discussion in

Section 3.3). The temperature increase is on a similar level for rectangular and semicircular shapes. All curves show a positive gradient at the end of the measuring time. The steady state has therefore not yet been reached.

Figure 5 shows the evolution of the temperature difference $\Delta\vartheta$ between the added reinforcement (T_1) and the initial cross-section with time at the level of the bar, 0.5 mm to the side of the slot edge (T_2), derived from temperature measurements in Figure 4. $\Delta\vartheta$ rises sharply at the beginning of the test, regardless of the slot shape, and then stabilizes on an approximately constant level after about 30 min. For the triangular shape, $\Delta\vartheta$, averaged over the period $t > 30$ min, is highest (~18°C), followed by the semicircular (~16°C) and the rectangular shape (~11°C).

FIGURE 6 Temperature distribution in the specimen with triangular-shaped slot at different times, measured with DFOS.
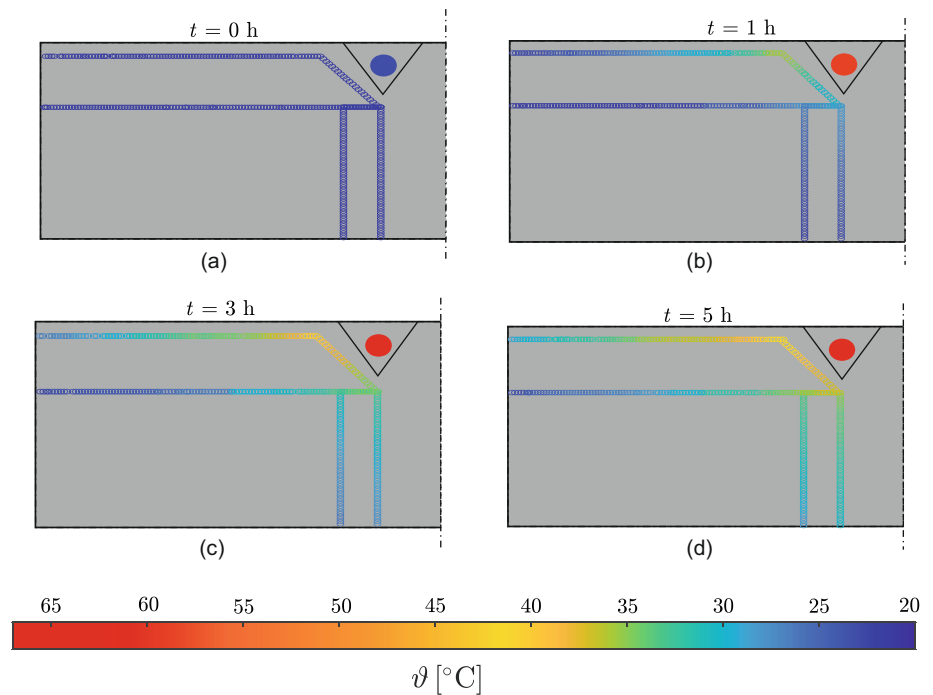
3.2 | Temperature distribution over the cross-section

The temperature distribution recorded by DFOS in the specimen with a triangular slot is shown for the times $t = [0, 1, 3, 5]$ h in Figure 6. At the beginning of the test ($t = 0$ h), the entire cross-section has an almost constant temperature of 20°C. After 1 h, the added bar has heated up to 58°C. In the initial cross-section, the temperature has only risen slightly to approximately 30–35°C directly around the slot. After $t = [3, 5]$ h, the rod has heated up further to [64, 66]°C. As the tempering time increases, the temperature rise in the initial cross-section also increases. The heat propagation is mainly concentrated on the side of the slot. Here the concrete has a temperature of approximately 40–45°C. Even after $t = 5$ h, the region below the slot experiences only a slight increase in temperature. While the temperature immediately below the slot rises to approximately 40°C, the deeper layers remain at approximately 25–30°C.

3.3 | Effect of the slot's shape on the achievable temperature of the bar

The shape of the slot influences both the temperature evolution of the added bar and the heat transfer to the concrete. The maximum bar temperatures $\vartheta_{s,max}$ reached in the tests after $t = 5$ h are summarized for the different slot shapes in Table 3. $\vartheta_{s,max}$ is 56°C for the

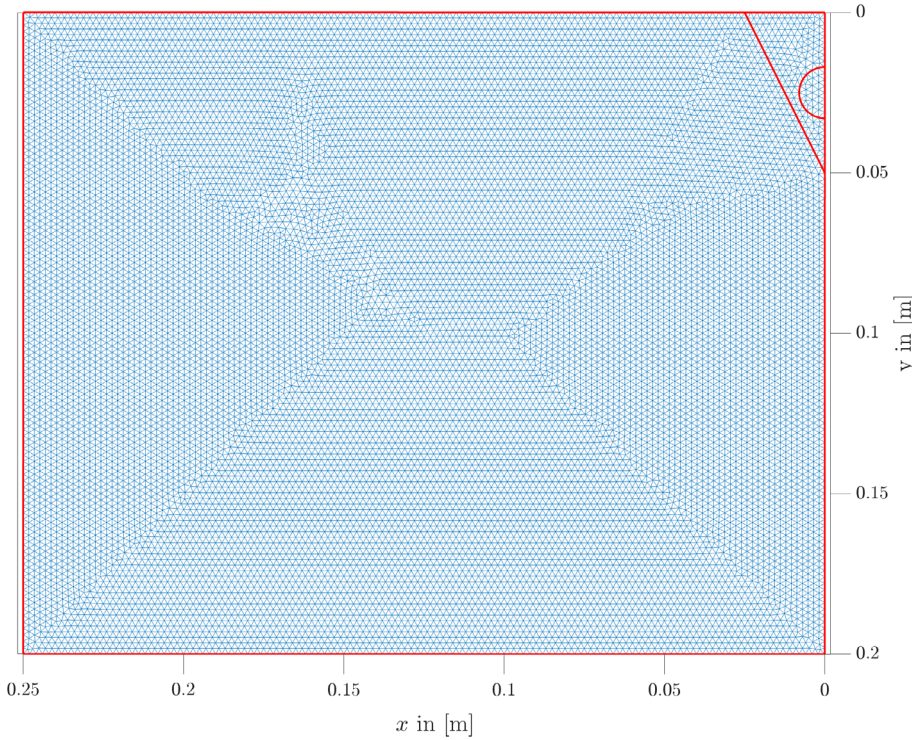rectangular shape, 60°C for the semicircular shape and 66°C for the triangular shape. The tempered surface A of the slot is 250 cm² regardless of the shape. Accordingly, the same heating mat is used in all tests. All other boundary conditions are also identical, which is why the temperature differences can be purely attributed to the slot shape.

The liquid HPC in the slot has a thermal conductivity coefficient $\lambda = 4.3$ W/(m K), while the hardened normal strength concrete of the initial cross-section has a $\lambda = 1.65$ W/(m K).[27] The latter therefore insulates the slot. The heat induced at the top of the slot spreads quite quickly in the more conductive, liquid HPC and is accumulated at the contact surface U to the concrete. The temperature $\vartheta_{s,max}$ in the slot increases. A low U thus causes an increase in temperature in the slot. This also applies to a low slot volume V to be heated with the same temperature-controlled surface A and therefore a low ratio V/A. Both V/A and U are lowest for the triangular shape (Table 3), which is why this shape is best suited for tempering subsequently added reinforcing bars.

Another advantage of the triangular shape is that the heat is concentrated at the tip due to the triangular shape and the concrete, which is a poor conductor of heat. The heat therefore dissipates mainly in the area near the surface via the sides of the triangle (Figure 6). In this case, cooling from the top represents a promising approach to counteract this. This is examined in the following sections, first numerically (Section 4) and then experimentally (Section 5).

TABLE 3 Influence of the slot shape on the maximum reached bar temperature.

Slot shape	Max. bar temperature $\vartheta_{s,max}$ [°C]	Tempered surface A [cm²]	Slot volume V [cm³]	Ratio V/A [cm³/cm²]	Contact area U [cm]
Rectangle	56	250	1250	5.0	15.0
Semicircular	60	250	803.4	3.3	12.9
Triangle	66	250	625	2.5	11.2

FIGURE 7 Sketch of the solution space of the heat equation and the discretization for numerical computation.

4 | NUMERICAL INVESTIGATIONS OF THE INDUCTION METHOD

4.1 | Numerical adaption

To investigate broader thermal and geometric boundary conditions as part of a parametric study, the test setup with a triangular slot is mapped digitally. The model captures the temperature distribution in the cross-section as well as the resulting thermal strains. These are used to derive the effective prestress of the added reinforcement, which serves as an evaluation criterion in subsequent investigations. The strain calculation is carried out by coupling a numerical temperature field simulation (2D) and an iterative cross-section calculation with a lamella model (1D).

The calculation of the transient temperature distribution $\vartheta(t, \boldsymbol{x})$ in the cross-section Ω along its boundaries Γ is performed using the two-dimensional equation of heat conduction according to[39]:

$$c_p \rho \partial_t \vartheta(t, \boldsymbol{x}) - \nabla \cdot (\lambda \nabla \vartheta(t, \boldsymbol{x})) = 0, \boldsymbol{x} \in \Omega, t > 0,$$
$$\vartheta(0, \boldsymbol{x}) = \vartheta_0, \boldsymbol{x} \in \Omega, t = 0, \tag{1}$$

where the initial material temperature ϑ_0, the heat capacity c_p, the density ρ and the thermal conductivity λ are given as thermal material parameters. The solution space Ω in Figure 7, with the boundaries $\Gamma = \bigcup_{i=1}^5 \Gamma_i$, consists of the initial cross-section Ω_1 as normal-strength concrete, the slot Ω_2 as HPC, and the added reinforcement Ω_3. The symmetry of the overall cross-section allows the temperature calculation to be limited to just one half of the cross-section, which significantly reduces calculation times.

The boundary conditions for (Equation 1) are derived according to

$$\lambda \nabla \vartheta = \dot{q}, \ \boldsymbol{x} \in \Gamma_1, \ t > 0, \tag{2}$$

$$\lambda \nabla \vartheta = \sigma_2(\vartheta - \vartheta_{2,\infty}), \ \boldsymbol{x} \in \Gamma_2, \ t > 0, \tag{3}$$

$$-\lambda \nabla \vartheta = \sigma_3(\vartheta - \vartheta_{3,\infty}), \ \boldsymbol{x} \in \Gamma_3, \ t > 0, \tag{4}$$

$$\lambda \nabla \vartheta = 0, \boldsymbol{x} \in \Gamma_4 \cup \Gamma_5, t > 0. \tag{5}$$

The heating mat is modeled by a heat flux $\dot{q}$ applied from the outside over the slot width. According to Fourier's law, see ref. [40], the energy supply through the heat flux at the boundary Γ_1 is described by means of a Neumann boundary condition (Equation 2). The temporal evolution of $\dot{q}$ was recorded in the experiment with a heat-flux sensor (Hukseflux FHF04SC, $h = 0.4$ mm) according to the setup in ref. [21] and is applied for the numerical calculation. In the experiment, the area between the slot and the cooling, here marked as Γ_2, is directly exposed to the air. The resulting convective heat transfer between the concrete and the ambient air is treated as a mixed boundary condition, taking into account the ambient air temperature $\vartheta_{2,\infty}$ and the heat transfer coefficient σ_2 (Equation 3). The cooling with dry ice at the edge Γ_3 can also be mathematically expressed by a mixed boundary condition (Equation 4), where $\vartheta_{3,\infty}$ represents the temperature of the dry ice and σ_3 the associated transfer coefficient. Ideally, neither energy input nor energy output occurs at the thermally insulated boundary Γ_4, so that this can be mathematically defined as a Neumann boundary condition (Equation 5). Similarly, it is assumed that $\dot{q} = 0$ applies to the heat flux at the boundary Γ_5, so that this is modeled as a Neumann boundary condition, too (Equation 5). All numerical values for the parameters $(\vartheta_{2,\infty}, \vartheta_{3,\infty}, \sigma_2, \sigma_3)$ are listed in Table 4.

The solution of the partial differential equation (1) with the boundary conditions (Equations 2–5) is determined numerically by means of the MATLAB PDE Toolbox.[41] To discretize the cross-section into finite elements

TABLE 4 Material parameters for the numerical temperature field simulation.

Parameter	Value	Unit	Range
ρ	2000	kg/m^3	Ω_1
ρ	2440	kg/m^3	Ω_2
ρ	7895	kg/m^3	Ω_3
λ	1.0	W/(K m)	Ω_1
λ	4.0	W/(K m)	Ω_2
λ	50	W/(K m)	Ω_3
c_p	1000	J/(kg K)	Ω_1
c_p	1300	J/(kg K)	Ω_2
c_p	500	J/(kg K)	Ω_3
$\vartheta_{2,\infty}$	20	°C	Γ_2
$\vartheta_{3,\infty}$	−78	°C	Γ_3
σ_2	10	W/(K m^2)	Γ_2
σ_3	70	W/(K m^2)	Γ_3

(FE), a grid with $n_e = 28{,}832$ triangular elements and $n_k = 58{,}117$ nodes is used (Figure 7), cf. ref. [40]. The triangular slot shape and the round reinforcement bar are approximated by elements with an edge length of 1 mm. The element size increases to a maximum of 2 mm at the non-tempered cross-sectional boundaries. According to refs. [26,27] the material-specific parameters of density ρ, thermal conductivity λ and specific heat capacity c_p are assigned to each element regarding the three materials used (Ω_1–Ω_3) (Table 4).

The finite element discretization results in the system of ordinary differential equations according to Equation (6)[40] with $C \in \mathbb{R}^{n_k \times n_k}$ the thermal damping matrix, $K \in \mathbb{R}^{n_k \times n_k}$ the thermal stiffness matrix, the input vector $\boldsymbol{b} \in \mathbb{R}^{n_k \times 1}$, and the vector $\boldsymbol{f} \in \mathbb{R}^{n_k \times 1}$, which summarizes the further influences of the boundary conditions from Equations (3)–(5).

$$\begin{aligned} C\,\dot{\boldsymbol{\vartheta}}(t) + K\boldsymbol{\vartheta}(t) &= \boldsymbol{b}\,\dot{q} + \boldsymbol{f}, \ \ t > 0, \\ \boldsymbol{\vartheta} &= \boldsymbol{\vartheta}_0, \ \ t = 0. \end{aligned} \tag{6}$$

In the time domain, Equation (6) is solved by an implicit solution algorithm over the time interval $t \in (0, \tau)$. The result is the transient temperature distribution $\vartheta(t)$ in the cross-section half over n_k nodes.

With α_T the resulting thermal strains in the cross-section are calculated from the temperature changes calculated at each node. For this, the calculated temperature values of the nodes irregularly spread over the cross-section (see Figure 7) are first transferred by linear interpolation between the elements to a regular temperature grid with a spacing of 1 cm in the x- and y-directions. Due to the symmetrical temperature distribution in the x direction and under the assumption of the Bernoulli hypothesis, a lamella model is used for calculation on the cross-section, cf.[42] The interpolated temperature changes are transferred into a mean temperature change for each row, from which the associated thermal strain $(\varepsilon = \overline{\Delta \vartheta} \cdot \alpha_T)$ is calculated. The resulting strain distribution, which is non-linear over the height of the initial cross-section, is decomposed into a constant $(\varepsilon_{c1,0})$ and a linear variable portion $(\varepsilon_{c1,lin}(z))$ according to refs. [26,43,44] The total strain of the initial cross-section is $\varepsilon_{c1}(z) = \varepsilon_{c1,0} + \varepsilon_{c1,lin}(z)$. A constant thermal strain ε_s is assumed for the added reinforcement, corresponding to a temperature change at its barycenter. According to the experimental setup in Figure 2, Figure 8 (left) color-codes the numerically calculated and subsequently interpolated temperature distributions on the cross-section without cooling for the times $t = [1–3]$ h. Warm regions are highlighted in red, cold ones in blue. The comparison with the temperature development measured at various points in the experiment (Figure 6) shows an average
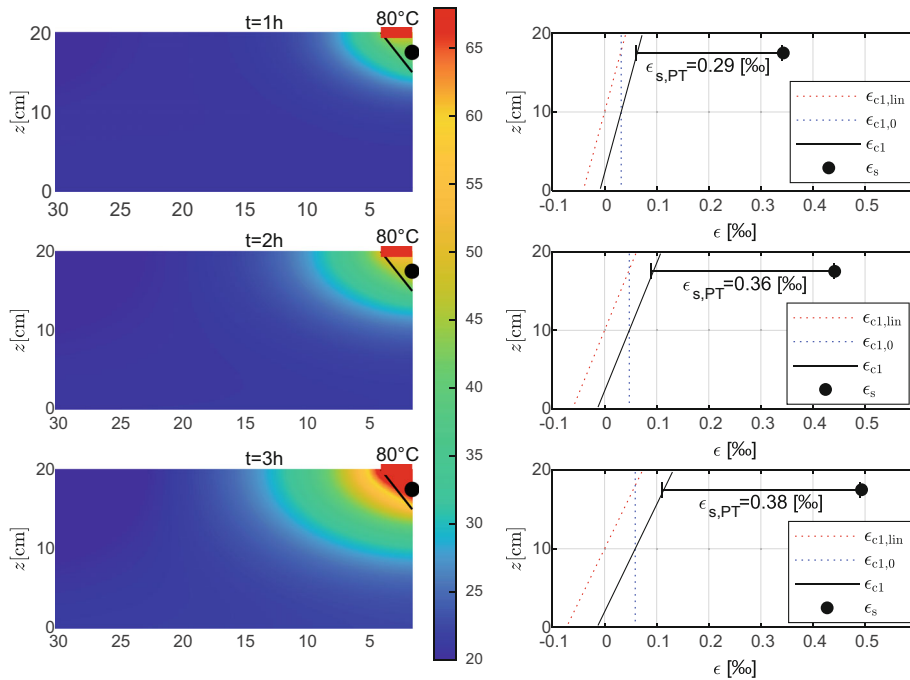
FIGURE 8   Calculated temperature distribution in the test specimen for various points in time (left) with the associated strain distribution in the initial cross-section and the added bar (right).

deviation of 1.9°C or approximately 4%. The resulting, linearized thermal strains in the initial cross-section and the added reinforcement due to the temperature distribution are shown in Figure 8 (right). $\varepsilon_{s,PT}$ results from the strain difference between the added reinforcement (ε_s) and the concrete in the corresponding lamella at the level of the reinforcement ($\varepsilon_{c1}(z = 17.5\,\text{cm})$). After 1 h, ε_s is 0.34‰. The corresponding thermal strain of the concrete $\varepsilon_{c1}(z = 17.5\,\text{cm})$ due to heat propagation reduces the effective strain $\varepsilon_{s,PT}$ to 0.29‰. With the tempering time, the temperature at the added bar rises and thus also ε_s. Due to its mass, the concrete reacts with delay to the heat supply and thus, its strain increases slower, too. Therefore, $\varepsilon_{s,PT}$ increases to 0.36‰ or 0.38‰. In fact, the target strain of 0.6‰ defined in Section 2 for which $\varepsilon_{s,PT} = \varepsilon_{s0}$, is never reached. The effectiveness of the strengthening ($\varepsilon_{s,PT}/\varepsilon_{s0}$) is 48%–63%. Further optimization of the induction method is thus necessary.

4.2 | Parameter study on the impact of thermal and geometric boundary conditions on the thermally generated pre-strain

In the framework of a parameter study, the developed numerical model is used to optimize the induction method with regard to $\varepsilon_{s,PT}$. The test setup shown in Figure 2 with a triangular slot is extended by a laterally offset cooling system on the upper side of the concrete using dry ice. The position and width of the cooling are variable. The thermal prestress results from the imprinted strains at the time when the HPC has hardened sufficiently to transmit the force. The investigations in Ref. [28] show that the condition for the HPC used is usually met after approximately 2 h. Accordingly, the strain $\varepsilon_{s,PT}$ (2 h) is evaluated and optimized in the course of the parameter study.

The influence of the distance n between the heating mat and the dry ice when cooling the cross-section up to the edge ($c = 30\,\text{cm}$) is shown in Figure 9 (left). For $n = 0\,\text{cm}$—cooling starts right from the heating mat— $\varepsilon_{s,PT}$ is 0.45‰. As n increases, so $\varepsilon_{s,PT}$ does. The maximum occurs for $n = n_{opt} = 6\,\text{cm}$ ($\varepsilon_{s,PT} = 0.60‰$). Beyond that, $\varepsilon_{s,PT}$ decreases again.

The influence of c (distance between the outer edge of the cooling and the center of the sample) on $\varepsilon_{s,PT}$ at $n = n_{opt}$ according to Figure 9 (left) is shown in Figure 9 (right). $c = 8.5\,\text{cm}$ ($n_{opt} + b'/2$) corresponds to no cooling. With c, $\varepsilon_{s,PT}$ rises, too.

The cooling of the initial cross-section effectively counteracts heating and leads to a significant increase of $\varepsilon_{s,PT}$. The target strain of 0.60‰ is now reached. Compared to the case without cooling (Figure 8), this corresponds to an increase in effectiveness of about 66%.

Besides the cooling, the slot dimensions are also optimized numerically. Figure 10 shows the influence of the slot width b' (left) and the slot depth h' (right) on $\varepsilon_{s,PT}$ in an otherwise unchanged test setup and the optimized cooling geometry according to Figure 9. Throughout, the slot is tempered over its entire width. As shown in Figure 10 (left) the tempered surface initially increases
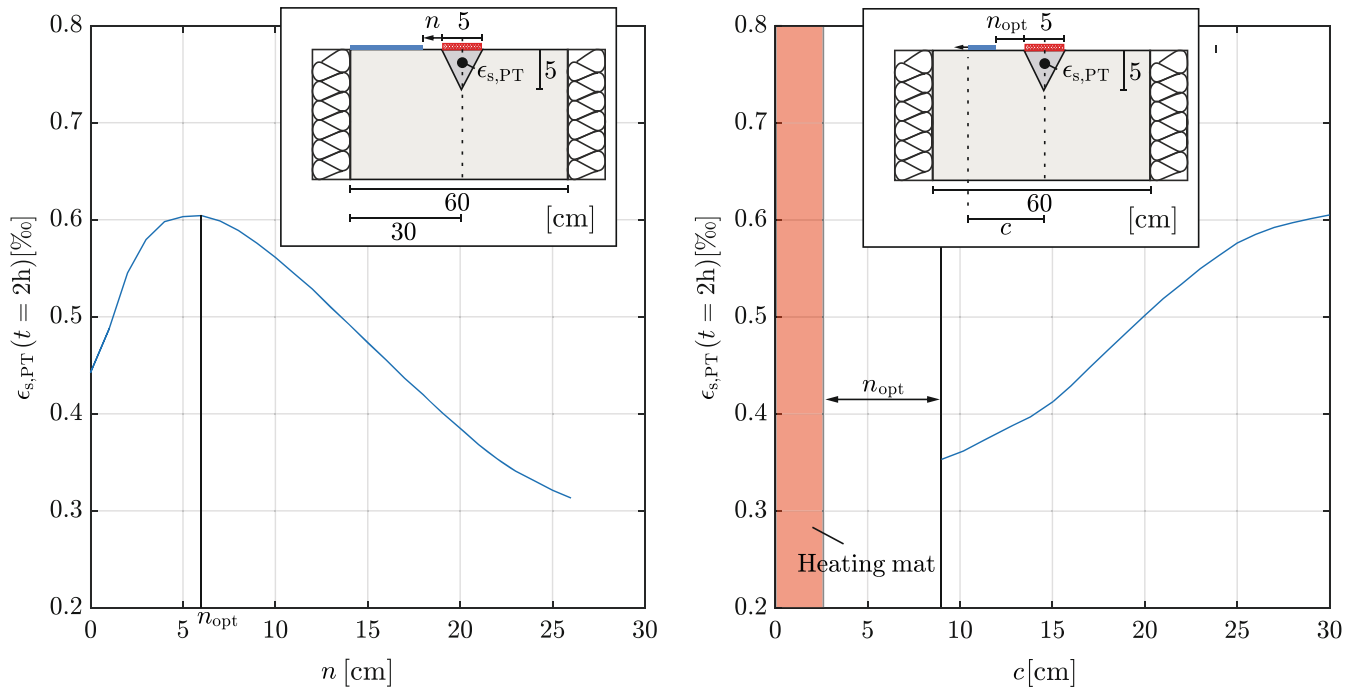
FIGURE 9   Influence of the cooling distance on the calculated prestress of the added reinforcing bar (left) and influence of the cooling width at an optimal cooling distance (right).
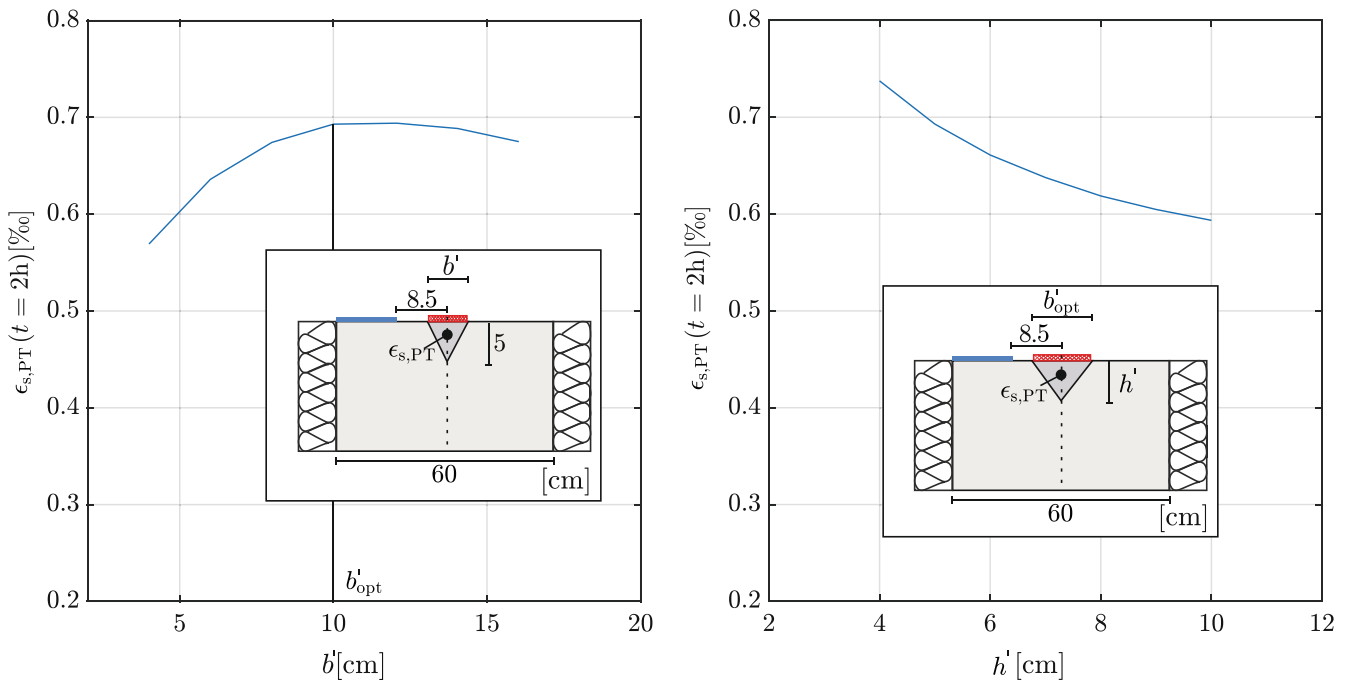

FIGURE 10   Influences of the slot width on the calculated thermal pre-strain of the added reinforcing bar (left) and of the slot depth at an optimized slot width (right).

with b', too. The maximum occurs at $b' = b'_{\text{opt}} = 10\,\text{cm}$ ($\varepsilon_{s,PT} = 0.69\,‰$). Beyond that, $\varepsilon_{s,PT}$ decreases again. The influence of the slot depth h' at b'_{opt} on $\varepsilon_{s,PT}$ is shown in Figure 10 (right). With decreasing h', $\varepsilon_{s,PT}$ increases. The

reason is that the slot volume V decreases while the tempered surface remains the same, which according to Section 3.3 leads to an increasing bar temperature and thus to an increase of $\varepsilon_{s,PT}$.

4.3 | Induction method for thermal pre-stressing of subsequently added reinforcement

The results of the experimentally and numerically developed induction method are summarized in Figure 11. The highest effectiveness of the strengthening measure results from bars in triangular slots with a width of 10 cm and a minimum depth. To ensure sufficient concrete cover of the bars, the slot depth for usual diameters (between 10 and 20 mm) is set to 5 cm. The slots should be exposed to a temperature of 95°C induced over their entire width at the component surface.

The lateral cooling of the concrete surface with dry ice reduces the temperature increase in the surrounding concrete and thus increases the effectiveness of the strengthening. The cooling is to be carried out at a distance of $n = 6$ cm from the slot and as wide as possible. In order to achieve 100% effectiveness of the strengthening ($\varepsilon_{s,PT} = 0.6‰$) with the selected boundary conditions (n_{opt}, b'_{opt}, and h') according to Section 4.2, $c > 20$ cm must apply. In practice, a structure is usually strengthened by slotting several reinforcement bars next to each other.

To ensure that the required cooling width is maintained for each bar, the required bar spacing is set to $2 \times c = 40$ cm (Figure 11a). Accordingly, it is recommended to maximize the bar spacings by preferring bigger diameters and at the same time to maintain the statically and constructively required bar spacings by adding the bars one after the other (Figure 11b). In the first step, for example, every second slot is created and a bar is placed in it. Cooling follows between the slots, maintaining the minimum width. After the cross-section has cooled completely, a further bar can be added between the already created slots in a second step, and the induction can be repeated.

5 | EXPERIMENTAL IMPLEMENTATION OF THE OPTIMIZED INDUCTION METHOD

5.1 | Validation of the numerical solution by experiment

The numerically optimized induction method according to Section 4.3 is implemented in an experiment for validation. The basic test setup and the measurement technology used correspond to Figure 2 with cooling. The slot width b' remains unchanged at 5 cm due to the available heating technology. The other boundary conditions (slot shape, h', n, c) correspond to Section 4.3. To ensure comparability of experiment and numerics, b' is also adapted in the model.

Figure 12 compares the temperature curves measured in the experiment with the thermocouples T_1, T_2, and T_4 with the numerically calculated curves at the same location. The calculated curves approximate the measured temperatures at the design-relevant time after $t = 2$ h with a maximum deviation of 2.5°C.

In the experiment, the temperature evolution in the test object is only measured at selected points. In order to determine the overall temperature distribution and calculate the resulting thermal strain according to Section 4.1, interpolation is performed between the measuring points. The principle is shown in Figure 13 (top left). The temperature evolution in the initial cross-section is known from the lateral DFOS measurements in two layers across the width. The DFOS measurements below the slot show that after about an hour, an approximately linear temperature distribution with 20°C at the lower edge has been established over the height of the specimen and that this remains unchanged over the entire duration of the test. Accordingly, a linear approach is chosen to interpolate between the two DFOS layers and the lower cross-sectional edge (assumed to have 20°C). The temperature distribution in the slot is also determined by interpolation
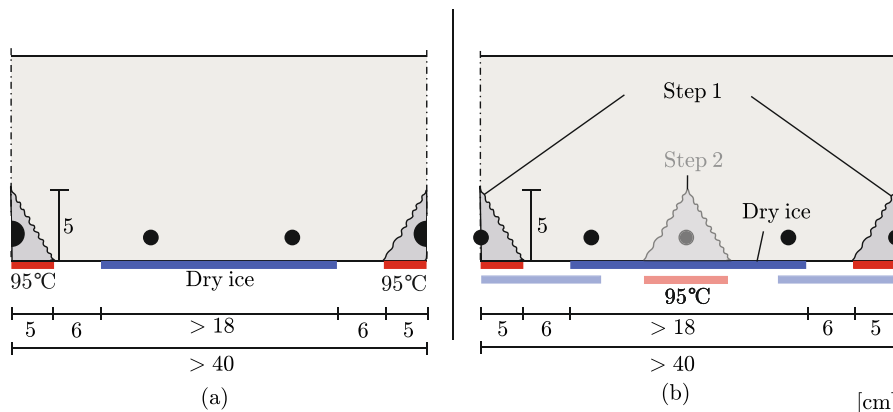

FIGURE 11 Setup of the optimized induction method with big bar diameters and slot spacings (a) and added bars in slots produced one after the other (b).
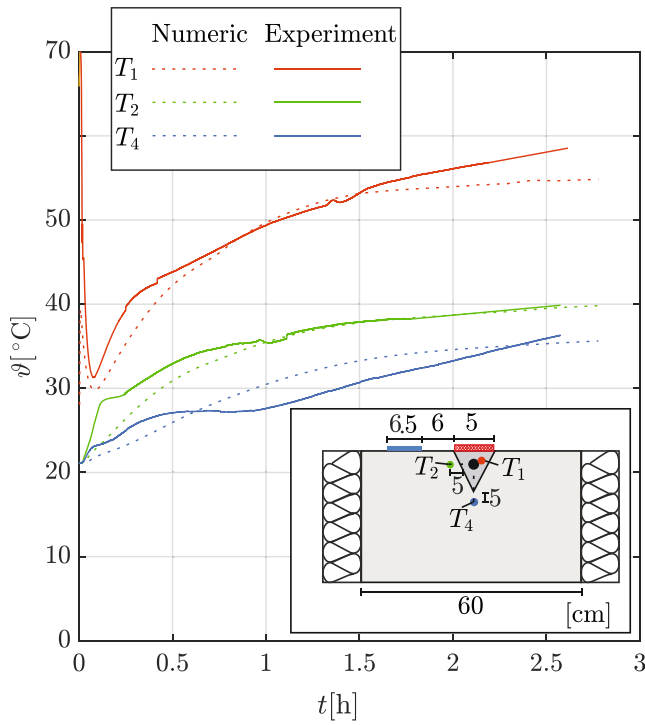
FIGURE 12 Comparison of the calculated temperature evolution in the specimen at three points with the measured temperature evolution for the test setup shown.

between the known temperatures at the sides of the slot, at the extended member, and at the tempered edge.

Figure 13 (left and center) shows the resulting temperature distributions in the specimen at times $t = [1\text{–}3]$ h. At $t = 1$ h, the region directly below the cooling exhibits a temperature of about $-40°C$, while the added bar has heated up to about $50°C$. The effective range of the dry ice cooling decreases with increasing tempering time. The temperature in the slot and the initial cross-section rises, and the cold region becomes smaller and shifts sideways away from the slot. The vertical DFOS measurements under the slot serve as a plausibility check for the interpolated temperatures. The comparison of the calculated and measured temperatures shows a maximum deviation of 5°C.

The temperature distributions in the initial cross-section are converted into linear strains ($\varepsilon_{c1,0}$ and $\varepsilon_{c1,lin}$) according to Section 4.1 (Figure 13, right). The strain of the added reinforcement ε_s is obtained directly from the temperature change measured there. $\varepsilon_{s,PT}(1\,h)$ is 0.40‰. With increasing tempering time, $\varepsilon_{s,PT}$ increases to 0.50‰ (2 h) or 0.49‰ (3 h). The numerical calculation for the test setup yields $\varepsilon_{s,PT}(2\,h) = 0.49$‰. The deviation between the numerical calculation and the experiment is therefore only 2%.
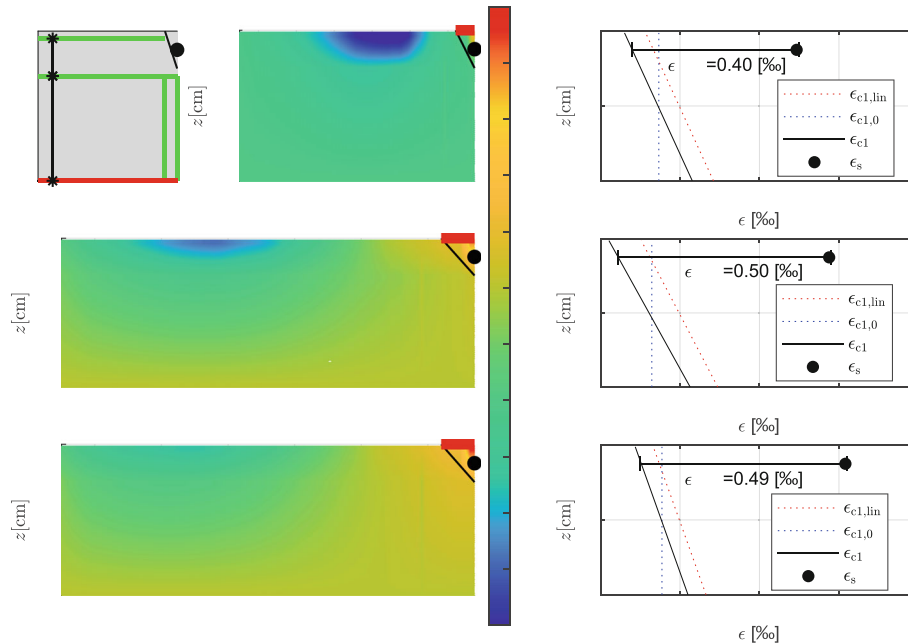

FIGURE 13 Linearly interpolated temperature distribution in the specimen, based on the temperature measured in the experiment using DFOS at different times (left) and the resulting strain distributions in the added bar and initial cross-section.

6 | CONCLUSIONS

The paper shows the experimental and numerical development of an induction method to strengthen reinforced concrete structures using thermally prestressed additional reinforcement. The main factors influencing the effectiveness of the strengthening are investigated by means of experimental tests and by coupling numerical temperature field simulation with a stress calculation at the cross-section level. The optimized induction method is derived from the results, taking into account practical construction aspects and validated in a further experiment. The main findings are:

- A triangular slot shape is best suited for thermal prestressing of the reinforcement bars inserted into it. In the tests, a higher bar temperature was achieved compared to a rectangular and a semicircular shapes, with otherwise the same boundary conditions. In addition, the interface to the initial cross-section, through which the heat dissipates into the concrete, is smaller than with the other shapes. This results in a greater temperature difference between the added reinforcement and the concrete and thus a higher effectiveness of the reinforcement.
- The effectiveness of the reinforcement is significantly increased by optimizing the induction method. It is recommended to add bars in a triangular slot with a width of 10 cm and a depth of 5 cm. The initial cross-section should also be cooled with dry ice. The cooling should be performed at a distance of 6 cm from the slot with the largest possible cooling width.
- In practice, the strengthening is achieved by slotting several reinforcement bars next to each other. It is recommended to add a few bars with big diameter in order to increase the slot spacing and thus also the possible cooling width. On the one hand, this increases the effectiveness of the strengthening and, on the other hand, reduces the amount of work involved, since fewer slots have to be made. Alternatively, the bars can also be added one after the other with a smaller spacing and thermally prestressed.
- To validate the numerically optimized induction method, it is implemented in an experiment. The comparison of the results shows that the deviation between the numerical values and the experiment is <2%.

ACKNOWLEDGMENT

FUNDING INFORMATION

DATA AVAILABILITY STATEMENT
The data that support the findings of this study are available from the corresponding author upon reasonable request.

ORCID
David Sanio https://orcid.org/0000-0002-2507-3578

REFERENCES

1. Ramana V, Ramana VPV, Kant T, Morton SE, Dutta PK, Mukherjee A, et al. Behavior of CFRPC strengthened reinforced concrete beams with varying degrees of strengthening. Compos Part B Eng. 2000;31(6–7):461–70. https://doi.org/10.1016/S1359-8368(00)00022-6
2. Granata MF, La Mendola L, Messina D, Recupero A. Assessment and strengthening of reinforced concrete bridges with half-joint deterioration. Struct Concr. 2023;24(1):269–87. https://doi.org/10.1002/suco.202200367
3. American Road & Transportation Builders Association. *Bridge Report.* 2024.
4. Bundesministerium für Digitales und Verkehr. *Brücken an Bundesfernstraßen – Bilanz und Ausblick.* 2022.
5. Täljsten B, Elfgren L. Strengthening concrete beams for shear using CFRP-materials: evaluation of different application methods. Compos Part B Eng. 2000;31(2):87–96. https://doi.org/10.1016/S1359-8368(99)00077-3
6. Huang Y, Grünewald S, Schlangen E, Luković M. Strengthening of concrete structures with ultra high performance fiber reinforced concrete (UHPFRC): a critical review. Construct Build Mater. 2022;336:127398. https://doi.org/10.1016/j.conbuildmat.2022.127398
7. RILEM Technical Committee. Design procedures for the use of composites in strengthening of reinforced concrete structures. Dordrecht: Springer; 2016.
8. Hoppe J, Sanio D, Hormel A, Schlede D, Rode S, Mark P. CO2-Bilanzierung bei Straßenbrücken – Ein Bewertungsansatz für die Planungsphase von Baumaßnahmen. Bauingenieur. 2024;99(11):354–65.
9. Gschösser F, Schneider R, Tautschnig A. Expanding boundaries – retrofitting measure vs. replacement – LCA study for a railway bridge. Zürich: vdf Hochschulverlag AG an der ETH Zürich; 2016.
10. Zhu Y, Zhang Y, Hussein HH, Chen G. Numerical modeling for damaged reinforced concrete slab strengthened by ultra-high performance concrete (UHPC) layer. Eng Struct. 2020;209:110031. https://doi.org/10.1016/j.engstruct.2019.110031
11. Feix J, Lechner J. A new post-installed reinforcement system to extend life time of existing structures as contribution to sustainability. ce/papers. 2023;6(5):981–9. https://doi.org/10.1002/cepa.2002

12. Randl N, Kunz J. Post-installed reinforcement connections at ultimate and serviceability limit states. Struct Concr. 2014; 15(4):563–74. https://doi.org/10.1002/suco.201300094

13. Su R, Siu WH, Smith ST. Effects of bolt–plate arrangements on steel plate strengthened reinforced concrete beams. Eng Struct. 2010;32(6):1769–78. https://doi.org/10.1016/j.engstruct.2010.02.028

14. Barnes RA, Baglin PS, Mays GC, Subedi NK. External steel plate systems for the shear strengthening of reinforced concrete beams. Eng Struct. 2001;23(9):1162–76. https://doi.org/10.1016/S0141-0296(00)00124-3

15. Su R, Zhu Y. Experimental and numerical studies of external steel plate strengthened reinforced concrete coupling beams. Eng Struct. 2005;27(10):1537–50. https://doi.org/10.1016/j.engstruct.2005.04.012

16. Szczepański K, Kotynia R. Bending moments redistribution in two-span reinforced concrete beams reinforced with FRP bars based on collected data research. Struct Concr. 2024;25(2): 1076–91. https://doi.org/10.1002/suco.202300329

17. Zhang Z, Li W, Guo X, Sun Q, Tian P, Wu Y. Development of theoretical model for predicting flexural behavior of GFRP reinforced concrete beams with CFRP grid-reinforced ECC. Struct Concr. 2024;25(1):583–602. https://doi.org/10.1002/suco.202201214

18. Ghobarah A, El-Attar M, Aly NM. Evaluation of retrofit strategies for reinforced concrete columns. Eng Struct. 2000; 22(5):490–501. https://doi.org/10.1016/S0141-0296(98)00137-0

19. Ivanyi G, Buschmeyer W. Reinforcement of prestressed concrete bridges with steel plates – application criteria. Beton Stahlbetonbau. 1992;87(11):265–71. https://doi.org/10.1002/best.199200460

20. Mostakhdemin Hosseini MR, Dias S, Barros J. Flexural strengthening of reinforced low strength concrete slabs using prestressed NSM CFRP laminates. Compos Part B Eng. 2016; 90:14–29. https://doi.org/10.1016/j.compositesb.2015.11.028

21. Bierbrauer K. Zur Ermittlung der Tragfähigkeit bestehender Brücken aus Stahlbeton: Abschätzung der Bewehrungsmengen. Beton Stahlbetonbau. 2005;100(S2):13–6. https://doi.org/10.1002/best.200590255

22. Löschmann J, Ahrens A, Dankmeyer U, Ziem E, Mark P. Methods to reduce the partial safety factor concerning deadloads of existing bridges. Beton Stahlbetonbau. 2017;112(8): 506–16. https://doi.org/10.1002/best.201700027

23. Löschmann J, Clauß F, Mark P. Strengthening of reinforced concrete structures with temperature induction. Beton Stahlbetonbau. 2020;115(10):746–57. https://doi.org/10.1002/best.202000038

24. Löschmann J, Mark P. Strengthening of beams or slabs using temperature induction. Struct Concr. 2022;23(5):2770–85. https://doi.org/10.1002/suco.202100469

25. Löschmann J, Stolzuoli N, Ahrens MA, Mark P. Steering of continuity stresses in beam structures by temperature induction. Eng Struct. 2021;229:111621. https://doi.org/10.1016/j.engstruct.2020.111621

26. Schwarz Y, Sanio D, Mark P. Calculation model for thermal pre-stressing of subsequentlyadded reinforcement. Beton Stahlbetonbau. 2024;119(12):894–907. https://doi.org/10.1002/best.202400050

27. Schwarz Y, Ratke D, Sanio D, Meurer T, Mark P. An experimental method to capture the thermal conductivity coefficient of fine-grained. Materials (Basel, Switzerland). 2024;17(9):2115. https://doi.org/10.3390/ma17092115

28. Schwarz Y, Sanio D, Mark P. Influence of heat treatment on the bond creep of high-strength concrete. Beton Stahlbetonbau. 2024;119(4):253–64. https://doi.org/10.1002/best.202300088

29. Sagmeister B. Maschinenteile aus zementgebundenem Beton. Berlin, Germany: Beuth Verlag; 2017.

30. ducrete GmbH. Technische Daten NANODUR®-Beton [online]. https://www.durcrete.de/uhpc-mit-nanodur [Zugriff am: 1. Mrz. 2024]

31. Deuse T, Mutke S, Parker F, Qvaeschning D, Wulff M. Nanotechnisch optimierte Bindemittel für die Herstellung von anwendungsfreundlichem Hochleistungsbeton. Beton. 2019;6:210–9.

32. Stindt J, Kempf L-A, Forman P, Breitenbücher R, Mark P. DEF of high-performance concrete with rapid, non-standard heat-treatment. Case Stud Constr Mater. 2023;19:e02289. https://doi.org/10.1016/j.cscm.2023.e02289

33. Stindt J, Forman P, Mark P. Influence of rapid heat treatment on the shrinkage and strength of high-performance concrete. Materials. 2021;14:15. https://doi.org/10.3390/ma14154102

34. Clauß F, Löschmann J, Ahrens MA, Mark P. Temperature induction into RC structures. Beton Stahlbetonbau. 2021; 116(7):539–50. https://doi.org/10.1002/best.202100010

35. Clauß F, Ahrens MA, Mark P. Thermo-mechanical experiments on reinforced concrete beams: assessing thermal, mechanical, and mixed impacts on fiber optic measurements. Struct Concr. 2022;23(6):3521–37. https://doi.org/10.1002/suco.202100890

36. Bednarski Ł, Sieńko R, Howiacki T, Zuziak K. The smart nervous system for cracked concrete structures: theory, design, research, and field proof of monolithic DFOS-based sensors. Sensors (Basel). 2022;22(22):8713. https://doi.org/10.3390/s22228713

37. Richter B, Herbers M, Marx S. Crack monitoring on concrete structures with distributed fiber optic sensors—toward automated data evaluation and assessment. Struct Concr. 2024; 25(2):1465–80. https://doi.org/10.1002/suco.202300100

38. Konertz D, Löschmann J, Clauß F, Mark P. Fiber optic sensing of strain and temperature fields. Bauingenieur. 2019;94(7–8): 292–300. https://doi.org/10.37544/0005-6650-2019-07-08-70

39. Jiji LM, Danesh-Yazdi AH. Heat conduction. Cham, Switzerland: Springer; 2024.

40. Zienkiewicz OC, Taylor RL, Zhu JZ. The finite element method: its basis and fundamentals. Vol 7. 7th ed. New York: Butterworth-Heinemann; 2013.

41. The MathWorks. 2024Partial Differential Equation Toolbox [online] [Zugriff am: 05.2024].

42. Sanio D, Ahrens MA, Mark P. Lifetime predictions of prestressed concrete bridges—evaluating parameters of relevance using Sobol' indices. Civ Eng Des. 2022;4(5–6):143–53. https://doi.org/10.1002/cend.202100009

43. Sanio D, Mark P, Ahrens MA. Computation of temperature fields on bridges. Beton Stahlbetonbau. 2017;112(2):85–95. https://doi.org/10.1002/best.201600068

44. Quast U. Spannungsabhängige und thermische Dehnungen. Beton Stahlbetonbau. 2009;104(9):616–8. https://doi.org/10.1002/best.200908247

AUTHOR BIOGRAPHIES

Yannik Schwarz, Ruhr-University Bochum, Institute of Concrete Structures, 44780 Bochum, Germany. Email: yannik.schwarz@rub.de.

Denis Ratke, Karlsruhe Institute of Technology, Digital Process Engineering, 76131 Karlsruhe, Germany. Email: denis.ratke@kit.edu.

David Sanio, Ruhr-University Bochum, Institute of Concrete Structures, 44780 Bochum, Germany. Email: david.sanio@rub.de.

Thomas Meurer, Karlsruhe Institute of Technology, Digital Process Engineering, 76131 Karlsruhe, Germany. Email: thomas.meurer@kit.edu.

Peter Mark, Ruhr-University Bochum, Institute of Concrete Structures, 44780 Bochum, Germany. Email: peter.mark@rub.de.